Applied Physics Letters ARTICLE scitation.org/journal/apl

The influence of threading dislocations propagating through an AlGaN UVC LED

Cite as: Appl. Phys. Lett. **120**, 162101 (2022); doi: 10.1063/5.0086034
Submitted: 21 January 2022 · Accepted: 26 March 2022 ·
Published Online: 18 April 2022

Douglas Cameron,[1,a)] Paul R. Edwards,[1] Frank Mehnke,[2,3] Gunnar Kusch,[4] Luca Sulmoni,[2] Marcel Schilling,[2] Tim Wernicke,[2] Michael Kneissl,[2] and Robert W. Martin[1]

AFFILIATIONS

[1]Department of Physics, SUPA, University of Strathclyde, Glasgow G4 0NG, United Kingdom
[2]Institute of Solid State Physics, Technische Universität Berlin, Hardenbergstr. 36, 10623 Berlin, Germany
[3]School of Electrical and Computer Engineering, Georgia Institute of Technology, Atlanta, Georgia 30332, USA
[4]Department of Materials Science and Metallurgy, University of Cambridge, Cambridge CB3 OFS, United Kingdom

[a)]Author to whom correspondence should be addressed: douglas.cameron@strath.ac.uk

ABSTRACT

During the epitaxy of AlGaN on sapphire for deep UV emitters, significant lattice mismatch leads to highly strained heterojunctions and the formation of threading dislocations. Combining cathodoluminescence, electron beam induced current and x-ray microanalysis reveal that dislocations with a screw component permeate through a state-of-the-art UVC LED heterostructure into the active region and perturb their local environment in each layer as growth progresses. In addition to acting as non-radiative recombination centers, these dislocations encourage high point defect densities and three-dimensional growth within their vicinity. We find that these point defects can add parasitic recombination pathways and compensate intentional dopants.

III-nitride semiconductors have already had resounding commercial success in the visible lighting market. By increasing the AlN content in the active regions of optoelectronic devices, we have the potential to widen band gaps and increase the energy of emission into the deep UV. This tunability could allow the development of devices emitting at specific short wavelengths[1] for important applications such as disinfection[2–4] or water purification.[5]

In practice, it has proved challenging to produce such short wavelength emitters, as their external quantum efficiencies dramatically decrease with increasing AlN content due to reductions in radiative recombination efficiency, carrier injection efficiency, and light extraction efficiency.[6,7] The influence of threading dislocations as well as the cumulative effects of surface imperfections in the various epitaxial layers of a UV LED result in lateral variations. How these inhomogeneities impact overall device performance remains unclear.[8]

In this Letter, we examine a 262 nm emitting AlGaN LED[9] using a combination of scanning electron microscopy techniques. The LED structure was grown by metalorganic vapor-phase epitaxy on an epitaxially laterally overgrown sapphire/AlN template with an average edge type threading dislocation density of 1.5×10^9 cm^{-2} and a screw type threading dislocation density of 3×10^7 cm^{-2}.[10] We began with a 1.2 μm thick silicon-doped (2.5×10^{18} cm^{-3})[11] $Al_{0.90}Ga_{0.10}N$ n-contact layer and an initial 40 nm barrier of $Al_{0.88}Ga_{0.12}N$, before depositing the triple quantum wells with 1 nm $Al_{0.47}Ga_{0.53}N$ and 5 nm thick $Al_{0.60}Ga_{0.40}N$ barriers. Above this, a 6 nm AlN electron blocking layer was followed by $Al_{0.80}Ga_{0.20}N/Al_{0.70}Ga_{0.30}N$ and $Al_{0.37}Ga_{0.63}N/Al_{0.20}Ga_{0.80}N$ p-superlattices. The structure concludes with a 40 nm thick layer of p-GaN.

Using a scanning electron microscope (SEM), we bombard our specimen with high energy primary electrons, each of which can generate thousands of electron-hole pairs through a scattering cascade. These electrons and holes may radiatively recombine, generating cathodoluminescence (CL) containing information regarding the electronic structure, crystal structure, and defect populations. In the case of nonradiative recombination, phonons can be generated instead.

Alternatively, in the presence of strong internal electric fields from p–n junctions, heterojunctions, or Schottky contacts, separation of these carriers may occur, decreasing recombination and enhancing the collection current. We can collect this electron beam induced current (EBIC) and gain insight into the space charge region and carrier transport therein. The EBIC can additionally be used to investigate the properties of grain boundaries and extended defects as well as identify doping variations due to their impact on local field strengths.[12–15]

Electron beam excitation will also lead to core electron ionization and the emission of characteristic x rays. By analyzing these x rays, we can obtain accurate compositional data (fractional uncertainty 0.02–0.03[16]).

Both EBIC and CL hyperspectral imaging were carried out within an FEI Quanta 250 field emission gun SEM. Our custom-built CL setup collects light perpendicular to the beam excitation through a reflecting objective. The spectrum is measured using a $\frac{1}{8}$ m spectrometer containing a 50 μm slit and a 600 lines/mm grating, paired with a cooled back-illuminated electron multiplying charge coupled device.[17] EBIC measurements utilized a Kleindiek nanoprobing system with two tungsten tips connected to triaxial wires to reduce noise. We terminate one of these outputs directly to earth, while the other is earthed via a low current amplifier.

Direct compositional analysis in the form of characteristic x-ray mapping was performed inside a JEOL JXA-8530F electron probe microanalyzer using both energy dispersive and wavelength dispersive x-ray spectrometers.[16] We additively combine both of these channels to increase our signal to noise. By utilizing channels from multiple spectrometers positioned at different angles, we also avoid any misleading effects from topographic shadowing.

For EBIC measurements, we examined our specimen in both plan-view and cross-sectional geometries. In the planar orientation, multiple effects combine to produce the EBIC images seen in Fig. 1. Large scale contrast features are due to the inhomogeneity of the *p*-GaN capping layer thickness [visible in the SE image in Fig. 1(a)], vertically displacing carrier generation volumes relative to the junction position. The thickness of this layer varies due to inhomogeneous step bunching processes.[18] The largest current will be induced when the generation volume has greatest overlap with the space charge region. For this reason, the contrast related to the capping layer thickness is inverted when we vary the acceleration voltage from 5 kV [Fig. 1(b)] to 20 kV [Fig. 1(c)] and is minimized at around 10 kV when energy deposition best matches the 140 nm depth of the QWs. Generally, higher acceleration voltages decrease spatial resolution in thick samples due to the larger volume of excess carriers generated. However, here relatively high resolution is maintained due to the EBIC signal being dominated by carriers generated in, or diffusing into, the junction volume.

At the higher acceleration voltages, a network of small hexagonal and dodecagonal rings is apparent in the EBIC contrast across the entire sample. This is evidence of an asymmetric junction, caused by the complex multilayer structure of our device. The electric field strengths shown by our simulations are dramatically different depending on depth.[19] The fields on both sides of the junction can also change somewhat independently due to pinning in intermediate layers. Our depth resolved measurement, therefore, implies that the origins of the hexagonal ring structure lie within the thick *n*-contact layer. The presence of these crystallographically aligned rings indicates local variations in electric field strengths and/or recombination efficiency. The presence of multiple tiers in these rings suggests a three dimensional growth mode of hillocks with the inclined slopes of these features influencing the aluminum nitride mole fraction as well as doping concentrations.[20]

Dark spots near the center of these rings are consistent with threading dislocations acting as recombination centers.[14,21] We anticipate these extended defects to be screw type threading dislocations based on previous electron channeling contrast imaging by Kusch *et al.* on polar *n*-AlGaN layers.[22–24] By counting the number of spots in each image, we can calculate a density of 3×10^7 cm^{-2}, exactly matching our previously stated estimation for screw dislocation density.

Cross-sectional EBIC (see supplementary material S1) reveals the presence of a secondary weaker junction at the AlN/AlGaN heterojunction near the substrate. This is caused by the bandgap discontinuity and polarization fields forming an additional depletion region.[25]

To assist in explaining our EBIC observations, complementary CL measurements were performed. Selective plasma etching enables us to study the full heterostructure as well as the *n*-contact layer in isolation. First, we discuss CL measurements on the *n*-contact region, where the emission spectrum is dominated by the band edge emission (≈222 nm). We fit a Gaussian function to this peak and then map out the fitted peak intensity and center wavelength as seen in Fig. 2. Hexagonal features with bright edges can clearly be distinguished, and the energy of the emission here is significantly red shifted (≈60 meV) relative to the center of the hexagons due to changing alloy composition. Another notable feature in the band edge emission is the presence of darker sixfold symmetric lines, intersecting slightly offset from the center of these hexagons. These are an additional consequence of the growth modes and subsequent preferential incorporation on distinct facets.[26–28]

In addition to the band edge emission, two broad low intensity defect bands are observed. These are known transitions between

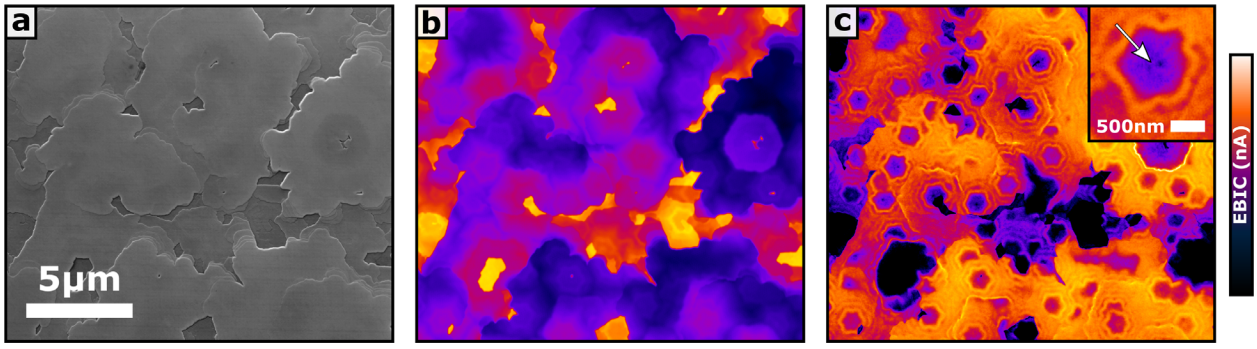

FIG. 1. Electron beam induced current measurements on the same area acquired at multiple acceleration voltages. (a) Secondary electron image of the area. EBIC images at (b) 5 kV and (c) 20 kV, including an inset to highlight an extended defect.

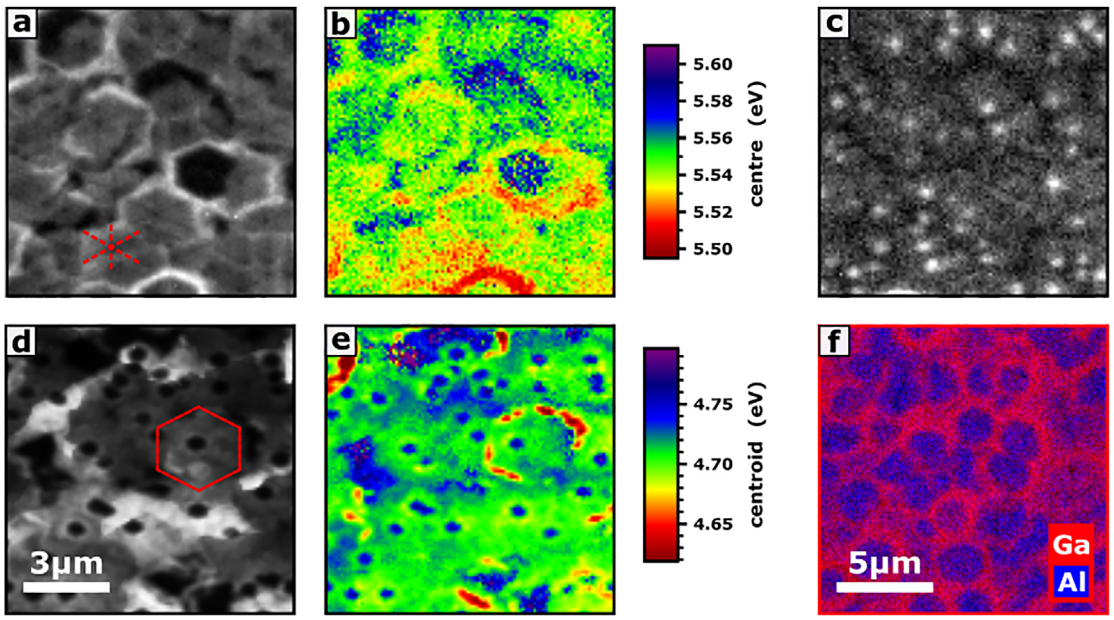

FIG. 2. CL and characteristic x-ray images. CL was mapped over 10 × 10 μm areas across both *n*-contact layer (a)–(c) and *p*-contact layer (d)–(e) using 6 kV. (a) The fitted intensity and (b) center energy of the band edge (222 nm) luminescence. (c) Defect luminescence band intensity (360–425 nm) in the *n*-contact layer. (d) Quantum well emission intensity (262 nm) and (e) emission energy maps. (f) Characteristic x-ray map of a 15 × 15 μm area of the *n*-contact layer with Ga shown in red and Al in blue.

shallow donors and two distinct deep acceptors.[29,30] The intensity of the first band lying between 250 and 310 nm follows that of the band edge emission. The second band (≈350–420 nm) shows brightest emission from clusters, which align precisely with the intersection of the sixfold lines where we expect a threading dislocation to be located. The density of the defect clusters observed in the *n*-layer [Fig. 2(c)] matches well with the hexagons observed in the EBIC image, and the formation of compensating defects may contribute to the decrease in the EBIC inside the small hexagons.

When measuring the full LED structure, the intensity of CL collected from the QWs is significantly modulated by variation in the absorbing capping layer with increasing thickness and decreasing the luminescence intensity due to absorption in this lower bandgap layer. We employ *p*-GaN due to the high resistivity of *p*-AlGaN, and in a final device, electroluminescence can freely escape via the sapphire substrate.[31] Despite this obscuration, we can still discern some larger hexagonal features with similar dimensions to those seen in the *n*-layers, relating to the GaN-rich regions. These appear with greater clarity in the centroid map, due to the redshift of the emission here. In addition, we see smaller hexagonal spots with low emission intensity and blue shifted energies. When compared with simultaneous EBIC data, these more numerous spots can be seen to align precisely with the ring structures previously described. The coincidence of low signals in both EBIC and CL confirms an increase in non-radiative recombination at the extended defects.

We have also mapped the characteristic x rays through the two surfaces. We note that although it is possible to quantify dopant concentrations using WDX,[16] mapping such small fluctuations is precluded by the x-ray count statistics. It also would fail to capture which of these dopants are actually electrically active.

Our measurements through the *p*-capping layer found no significant variation. However, the x-ray maps of the *n*-contact layer [shown in Fig. 2(f)] uncover clear Ga-rich rings and Al-rich spots, confirming that the red-shifted, high intensity luminescence we observed in the hyperspectral CL is related to changes in the alloy composition. Our results are consistent with previous works,[8,20,32,33] where it has been shown that hexagonal platelets with Ga-rich extremities develop during polar AlGaN growth due to the differences in mobilities between the Al and Ga ions[34] with the locations of the platelets being dictated by threading dislocations with a screw component.

In conclusion, we have employed EBIC, CL, and x-ray microanalysis to show that threading dislocations with a screw component originating in the preliminary layers of our UVC LED heterostructure persist into the active regions. In each of the penetrated layers, higher point defect densities and three-dimensional growth enclose the threading dislocations. These point defects can compensate electrical dopants and increase parasitic recombination by reducing the quantum well emission intensity. We find that during growth, the emergence of multiple facets with distinct incorporation rates leads to alloy composition and doping fluctuations, resulting in hexagonal structures interconnecting and forming a network visible in EBIC, CL, and characteristic x-ray maps. These results demonstrate the importance of controlling the density of these extended defects in preliminary layers due to their deleterious effects on the performance of optoelectronic devices.

See the supplementary material for a cross-sectional EBIC image showing the second space charge region, AFM images of a comparative *n*-contact layer, and CL spectra from the full LED and the *n*-contact layer.

We thank Sylvia Hagedorn and Markus Weyers (FBH) for providing ELO AlN/sapphire substrates and Praphat Sonka for operating the MOVPE system. This research was partially supported by the U.K. EPSRC (Nos. EP/R03480X/1 and EP/T023198/1) and the BMBF through funding in Advanced UV for life projects.

AUTHOR DECLARATIONS

Conflict of Interest

The authors have no conflicts to disclose.

DATA AVAILABILITY

The data is now available at https://doi.org/10.15129/333c40b0-bb43-48ce-8e9c-af420ef684d7.

REFERENCES

[1]M. Kneissl, T.-Y. Seong, J. Han, and H. Amano, "The emergence and prospects of deep-ultraviolet light-emitting diode technologies," Nat. Photonics **13**, 233 (2019).
[2]M. Raeiszadeh and B. Adeli, "A critical review on ultraviolet disinfection systems against COVID-19 outbreak: Applicability, validation, and safety considerations," ACS Photonics **7**, 2941 (2020).
[3]H. Inagaki, A. Saito, H. Sugiyama, T. Okabayashi, and S. Fujimoto, "Rapid inactivation of SARS-CoV-2 with deep-UV LED irradiation," Emerging Microbes Infect. **9**, 1744 (2020).
[4]J. Glaab, N. Lobo-Ploch, H. K. Cho, T. Filler, H. Gundlach, M. Guttmann, S. Hagedorn, S. B. Lohan, F. Mehnke, J. Schleusener *et al.*, "Skin tolerant inactivation of multiresistant pathogens using far-UVC LEDs," Sci. Rep. **11**, 14647 (2021).
[5]M. Würtele, T. Kolbe, M. Lipsz, A. Külberg, M. Weyers, M. Kneissl, and M. Jekel, "Application of GaN-based ultraviolet-C light emitting diodes–UV LEDs–for water disinfection," Water Res. **45**, 1481 (2011).
[6]H. Amano, R. Collazo, C. De Santi, S. Einfeldt, M. Funato, J. Glaab, S. Hagedorn, A. Hirano, H. Hirayama, R. Ishii *et al.*, "The 2020 UV emitter roadmap," J. Phys. D **53**, 503001 (2020).
[7]N. Maeda and H. Hirayama, "Realization of high-efficiency deep-UV LEDs using transparent p-AlGaN contact layer," Phys. Status Solidi C **10**, 1521 (2013).
[8]D. Liu, S. J. Cho, H. Zhang, C. R. Carlos, A. R. Kalapala, J. Park, J. Kim, R. Dalmau, J. Gong, B. Moody *et al.*, "Influences of screw dislocations on electroluminescence of AlGaN/AlN-based UVC LEDs," AIP Adv. **9**, 085128 (2019).
[9]M. Guttmann, F. Mehnke, B. Belde, F. Wolf, C. Reich, L. Sulmoni, T. Wernicke, and M. Kneissl, "Optical light polarization and light extraction efficiency of AlGaN-based LEDs emitting between 264 and 220 nm," Jpn. J. Appl. Phys., Part 1 **58**, SCCB20 (2019).
[10]N. Susilo, S. Hagedorn, D. Jaeger, H. Miyake, U. Zeimer, C. Reich, B. Neuschulz, L. Sulmoni, M. Guttmann, F. Mehnke *et al.*, "AlGaN-based deep UV LEDs grown on sputtered and high temperature annealed AlN/sapphire," Appl. Phys. Lett. **112**, 041110 (2018).
[11]I. Prozheev, F. Mehnke, T. Wernicke, M. Kneissl, and F. Tuomisto, "Electrical compensation and cation vacancies in Al rich Si-doped AlGaN," Appl. Phys. Lett. **117**, 142103 (2020).
[12]D. Holt, B. Raza, and A. Wojcik, "EBIC studies of grain boundaries," Mater. Sci. Eng., B **42**, 14 (1996).
[13]H. Leamy, "Charge collection scanning electron microscopy," J. Appl. Phys. **53**, R51 (1982).
[14]E. Yakimov, "Electron-beam-induced-current study of defects in GaN; experiments and simulation," J. Phys.: Condens. Matter **14**, 13069 (2002).
[15]M. Wallace, P. Edwards, M. Kappers, M. Hopkins, F. Oehler, S. Sivaraya, D. Allsopp, R. Oliver, C. Humphreys, and R. Martin, "Bias dependence and correlation of the cathodoluminescence and electron beam induced current from an InGaN/GaN light emitting diode," J. Appl. Phys. **116**, 033105 (2014).
[16]L. Spasevski, B. Buse, P. Edwards, D. Hunter, J. Enslin, H. Foronda, T. Wernicke, F. Mehnke, P. J. Parbrook, M. Kneissl *et al.*, "Quantification of trace-level silicon doping in $Al_xGa_{1-x}N$ films using wavelength-dispersive x-ray microanalysis," Microsc. Microanal. **27**, 696 (2021).
[17]P. R. Edwards, L. Krishnan Jagadamma, J. Bruckbauer, C. Liu, P. Shields, D. Allsopp, T. Wang, and R. W. Martin, "High-resolution cathodoluminescence hyperspectral imaging of nitride nanostructures," Microsc. Microanal. **18**, 1212 (2012).
[18]N. Susilo, J. Enslin, L. Sulmoni, M. Guttmann, U. Zeimer, T. Wernicke, M. Weyers, and M. Kneissl, "Effect of the GaN: Mg contact layer on the light-output and current-voltage characteristic of UVB LEDs," Phys. Status Solidi A **215**, 1700643 (2018).
[19]J. Glaab, J. Haefke, J. Ruschel, M. Brendel, J. Rass, T. Kolbe, A. Knauer, M. Weyers, S. Einfeldt, M. Guttmann *et al.*, "Degradation effects of the active region in UV-C light-emitting diodes," J. Appl. Phys. **123**, 104502 (2018).
[20]L. Spasevski, G. Kusch, P. Pampili, V. Z. Zubialevich, D. V. Dinh, J. Bruckbauer, P. R. Edwards, P. J. Parbrook, and R. W. Martin, "A systematic comparison of polar and semipolar Si-doped AlGaN alloys with high AlN content," J. Phys. D. Phys. **54**, 035302 (2021).
[21]J. Lähnemann, V. M. Kaganer, K. K. Sabelfeld, A. E. Kireeva, U. Jahn, C. Chèze, R. Calarco, and O. Brandt, "Carrier diffusion in GaN–a cathodoluminescence study. III: Nature of nonradiative recombination at threading dislocations," Phys. Rev. Applied **17**(2), 024019 (2020).
[22]G. Kusch, M. Nouf-Allehiani, F. Mehnke, C. Kuhn, P. R. Edwards, T. Wernicke, A. Knauer, V. Kueller, G. Naresh-Kumar, M. Weyers *et al.*, "Spatial clustering of defect luminescence centers in Si-doped low resistivity Al0.82Ga0.18N," Appl. Phys. Lett. **107**, 072103 (2015).
[23]S. Mita, R. Collazo, A. Rice, R. Dalmau, and Z. Sitar, "Influence of gallium supersaturation on the properties of GaN grown by metalorganic chemical vapor deposition," J. Appl. Phys. **104**, 013521 (2008).
[24]B. Heying, E. Tarsa, C. Elsass, P. Fini, S. DenBaars, and J. Speck, "Dislocation mediated surface morphology of GaN," J. Appl. Phys. **85**, 6470 (1999).
[25]M. Brendel, M. Helbling, A. Knigge, F. Brunner, and M. Weyers, "Measurement and simulation of top-and bottom-illuminated solar-blind AlGaN metal-semiconductor-metal photodetectors with high external quantum efficiencies," J. Appl. Phys. **118**, 244504 (2015).
[26]I. Girgel, P. R. Edwards, E. L. Boulbar, P.-M. Coulon, S. L. Sahonta, D. W. Allsopp, R. W. Martin, C. J. Humphreys, and P. A. Shields, "Investigation of indium gallium nitride facet-dependent nonpolar growth rates and composition for core–shell light-emitting diodes," J. Nanophotonics **10**, 016010 (2016).
[27]V. Kueller, A. Knauer, F. Brunner, U. Zeimer, H. Rodriguez, M. Kneissl, and M. Weyers, "Growth of AlGaN and AlN on patterned AlN/sapphire templates," J. Cryst. Growth **315**, 200 (2011).
[28]Z. Herro, D. Zhuang, R. Schlesser, and Z. Sitar, "Growth of AlN single crystalline boules," J. Cryst. Growth **312**, 2519 (2010).
[29]N. Nepal, M. Nakarmi, J. Lin, and H. Jiang, "Photoluminescence studies of impurity transitions in AlGaN alloys," Appl. Phys. Lett. **89**, 092107 (2006).
[30]T. Koppe, H. Hofsäss, and U. Vetter, "Overview of band-edge and defect related luminescence in aluminum nitride," J. Lumin. **178**, 267 (2016).
[31]M. Guttmann, A. Susilo, L. Sulmoni, N. Susilo, E. Ziffer, T. Wernicke, and M. Kneissl, "Light extraction efficiency and internal quantum efficiency of fully UVC-transparent AlGaN based LEDs," J. Phys. D **54**, 335101 (2021).
[32]Y. Saito, S. Wada, K. Nagata, H. Makino, S. Boyama, H. Miwa, S. Matsui, K. Kataoka, T. Narita, and K. Horibuchi, "Efficiency improvement of AlGaN-based deep-ultraviolet light-emitting diodes and their virus inactivation application," Jpn. J. Appl. Phys., Part 1 **60**, 080501 (2021).
[33]K. Uesugi, K. Shojiki, Y. Tezen, Y. Hayashi, and H. Miyake, "Suppression of dislocation-induced spiral hillocks in MOVPE-grown AlGaN on face-to-face annealed sputter-deposited AlN template," Appl. Phys. Lett. **116**, 062101 (2020).
[34]U. Zeimer, V. Kueller, A. Knauer, A. Mogilatenko, M. Weyers, and M. Kneissl, "High quality AlGaN grown on ELO AlN/sapphire templates," J. Cryst. Growth **377**, 32 (2013).